JOURNAL OF GEOPHYSICAL RESEARCH, VOL. 110, C02023, doi:10.1029/2004JC002569, 2005

Wave-current bedform scales, orientation, and migration on Sable Island Bank

C. E. Smyth[1] and M. Z. Li

Bedford Institute of Oceanography, Geological Survey of Canada–Atlantic, Dartmouth, Nova Scotia, Canada

Received 30 June 2004; revised 30 September 2004; accepted 19 January 2005; published 23 February 2005.

[1] Field observations of wave-current bedforms on Sable Island Bank show that medium to large bedforms were generally aligned with the wave direction, and did not follow the rotating tidal current. Normalized bedform heights and wavelengths were larger than predictions by Nielsen (1992), but agreed well with predictions by Khelifa and Ouellet (2000) which includes current effects. Maximum observed bedform wavelengths of 1.9 m were larger than those predicted for bedforms in wave-dominated nearshore conditions, but this may be expected as the water depths are larger (20–42 m) and currents are present. Measured bedform migration rates had higher vector correlation amplitudes when compared to significant wave velocity than with current velocity or skewness. Migration rate predictions from three presently available models were not able to predict net migration rate and direction in all cases.

Citation: Smyth, C. E., and M. Z. Li (2005), Wave-current bedform scales, orientation, and migration on Sable Island Bank, *J. Geophys. Res.*, *110*, C02023, doi:10.1029/2004JC002569.

1. Introduction

[2] There are few reported field measurements linking bedform migration to wave and current forcing. In wave-dominated regimes, several field observations have shown that bedform migration is well correlated with wave skewness [*Crawford and Hay*, 2001; *Traykovski et al.*, 1999]. In current-dominated regimes, bedforms have been observed to migrate in the direction of the current [*Ngusaru and Hay*, 2004; *Gallagher et al.*, 1998]. In the case of similar-strength wave-current forcing, *Ngusaru and Hay* [2004] found that cross-shore migration of lunate megaripples agreed with model predictions in which the wave and current shear stresses were added vectorially. Similarly, in field observations in slightly deeper water, *Li et al.* [1997] found that ripple migration direction was generally correlated with the combined wave and current shear stress. However, *Gallagher et al.* [1998] found that the direction of megaripples (often slightly lunate shaped) was not correlated with the direction of the vector sum of the wave and current velocities, but was aligned such that gross sediment transport normal to the bedform was maximized.

[3] Much of the difficulty in predicting bedload transport in combined flows is that the interactions between wave/current forcing, turbulence processes, and mobile beds are not well understood. Models simplify turbulence processes by using eddy viscosities and/or friction factors which are not well known for field conditions with irregular waves, tidal currents, complex bed topography, and mixed sediments.

[4] In this study, measurements of bedform dimensions, orientation, and migration rates were made on Sable Island Bank in water depths of 20–42 m over fine and coarse sand. In comparison to previous studies, present observations have a wider range of incident wave angles as well as a wider range of angles between waves and currents due to rotating tidal currents. Measured bedform migration rates are compared to wave/current forcing, and to predictions from three previously available models. These models include one bed stress model and two sediment transport models.

[5] Bedform geometry is also considered in this study. Present observations of bedform height and wavelength are compared to wave-dominated nearshore measurements and to combined-flow laboratory measurements.

[6] The next section briefly outlines the governing equations from the three selected models. A summary of the experiments, instrumentation, and data is found in section 3 along with forcing time series and forcing parameter definitions. Section 4 presents bedform dimension observations with comparisons to previous results. Section 5 includes measured bedform migration rates and comparison to model predictions and wave/current forcing.

2. Theory and Model Formulation

[7] Bedform migration velocity, $\mathbf{U_m}$, is related to volumetric bedload transport rate per unit width $\mathbf{Q_B}$ following *Bagnold* [1946],

$$\mathbf{U_m} = \frac{\mathbf{Q_B}}{\eta(1-\epsilon)}, \tag{1}$$

[1]Now at Department of Oceanography, Dalhousie University, Halifax, Nova Scotia, Canada.

0148-0227/05/2004JC002569$09.00

where η is the bedform height and ϵ is the sediment porosity. This model is based on desert sand dune migration in which dune advancement is accomplished by sand avalanche down the steep front face, and assumes bedform shape and migration rate are constant. This equation has been adopted for sediment transport in steady currents and wave-current environments, but sediment transport may not be accurately predicted if there is significant suspended load. Three models selected from the literature were used to predict bedload transport rates, and the above equation was used to estimate bedform migration rates for comparison to measurements.

[8] The first model, by *Ngusaru and Hay* [2004] (hereinafter NH04), relates bedload transport to the bottom stress, $\boldsymbol{\tau_b}$, by

$$\langle \mathbf{Q_B} \rangle = \hat{A}\left\langle \tau_b^{\xi-1}\boldsymbol{\tau_b} \right\rangle, \tag{2}$$

where $\hat{A}$ is an empirical constant, τ_b is the stress magnitude, ξ is taken as either 3/2 or 5/2, and $\langle\ \rangle$ represents a time average. Bed shear stress for combined waves and currents was taken as the vector sum of wave and current shear stresses following *Christoffersen and Jonsson* [1985] and *Sleath* [1995].

[9] The mean current shear stress is

$$\boldsymbol{\tau_c} = \frac{\rho}{2} f_c U_c \boldsymbol{U}, \tag{3}$$

where ρ is the fluid density, f_c is the current friction factor, and $\mathbf{U}$ is the horizontal current velocity with magnitude U_c given by $U_c^2 = U_x^2 + U_y^2$ with subscripts x and y denoting (x, y) components. As the shoreline is distant, for the present experiments, x is defined positive toward magnetic north, and y is defined positive to the east. Wave shear stress components are

$$\boldsymbol{\tau_w} = \frac{\rho}{2} f_w u_{wo} \boldsymbol{u}_w, \tag{4}$$

where f_w is the wave friction factor, u_{wo} is the wave orbital velocity amplitude, and $\boldsymbol{u_w}$ is the horizontal wave velocity. Instead of choosing friction factors, NH04 arranged the equations to obtain friction factors from best fits to their observations of lunate mega-ripple migration.

[10] *Christoffersen and Jonsson* [1985] (hereinafter CJ85) assume that the combined-flow bed stress is the vector sum of wave and current stresses. In their bed stress model, the governing equation for the current motion is

$$\rho\epsilon_c \frac{\partial \mathbf{U}}{\partial z} = \boldsymbol{\tau_c}(1 - z/h), \tag{5}$$

where ϵ_c is the eddy viscosity in the current boundary layer, z is the vertical coordinate positive up, and h is the water depth. The current shear stress is the same as in equation (3). The current friction factor for combined current wave motion is defined by

$$\sqrt{\frac{2}{f_c}} = \frac{1}{\kappa}\ln\frac{30h}{ek_N} - \frac{1}{\kappa}\ln\frac{k_A}{k_N}, \tag{6}$$

where κ is the von Kármán constant, h is the depth, and k_A is apparent roughness which is larger than the Nikuradse roughness, k_N, owing to the effect of the waves. Within the wave boundary layer, the governing equation in the wave component of the momentum equation is

$$\frac{\partial}{\partial t}(\mathbf{u_w} - \mathbf{u_{wb}}) = \frac{\partial}{\partial z}\left(\epsilon_w \frac{\partial \mathbf{u_w}}{\partial z}\right), \tag{7}$$

where ϵ_w is the eddy viscosity, and $\mathbf{u_{wb}}$ is the horizontal wave orbital velocity at the top of the wave boundary layer. Solutions of the governing equations are matched at the top of the wave boundary layer assuming eddy viscosity profiles. The wave shear stress is defined as in equation (4). The wave friction factor is given by

$$\frac{m}{4.07\sqrt{mf_w}} + \log\frac{1}{4.07\sqrt{mf_w}} = -0.1164 + \log\left(\frac{A\omega_r}{k_N\omega_a}\right), \tag{8}$$

where m is the ratio of the total bed shear stress to the wave component of the shear stress, A is the wave orbital semi-excursion, ω_a is the absolute wave angular frequency, and ω_r is the relative wave angular frequency. Wave and current friction factors are iteratively solved to convergence, and then the maximum bed stress is given by

$$\tau_b = \frac{mf_w\rho}{2} u_{wb}^2. \tag{9}$$

As this model does not include a bedload transport component, equation (2) was used to estimate bedload transport using the combined wave-current maximum bed stress.

[11] The third model was Sedtrans96 by *Li and Amos* [2001] (hereinafter LA01), which uses boundary layer theory by *Grant and Madsen* [1986]. Bedload transport is estimated using the Einstein-Brown bedload equation [*Brown*, 1950; *Madsen and Grant*, 1976],

$$\mathbf{Q_B} = 40 w_s d_{50}\left(\frac{1}{(\rho_s - \rho) g d_{50}}\right)^3 \tau_b^2 \boldsymbol{\tau_b}, \tag{10}$$

where w_s is the fall velocity, g is acceleration due to gravity, d_{50} is the mean grain size, and ρ_s is the sediment density. The combined shear stress, $\boldsymbol{\tau_b}$, was taken as grain roughness wave and current shear stresses added vectorially. These shear stress components are solved by iterating the following equations to convergence. An initial value of C_r, the wave to current ratio, is chosen, and the combined wave current friction factor is estimated from

$$\frac{1}{4\sqrt{f_{cw}}} + \log\frac{1}{4\sqrt{f_{cw}}} = \log\frac{12C_r u_w}{\omega d_{50}} + 0.14\left(4\sqrt{f_{cw}}\right) - 1.65, \tag{11}$$

where bottom roughness of $2.5d_{50}$ is assumed. Wave shear velocity, u_{*w} is estimated from

$$u_{*w} = \sqrt{\frac{C_r f_{cw}}{2} u_w^2}, \tag{12}$$

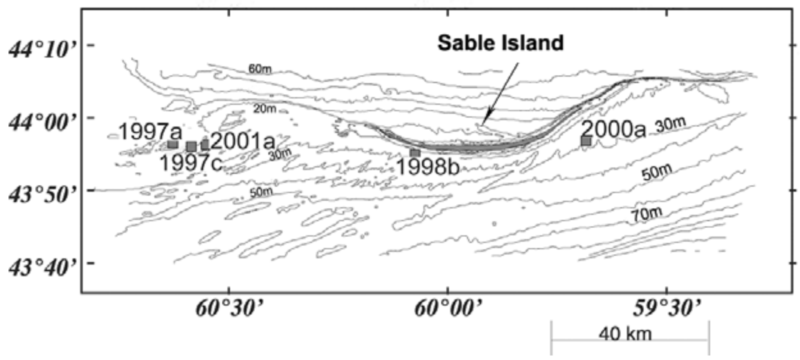

Figure 1. Bathymetry around Sable Island and deployment locations.

and the current shear velocity, u_{*c}, is estimated from matching velocity profiles at the top of the wave current boundary layer ($z = \delta_{wc}$),

$$U(z) = \frac{u_* c}{\kappa}\left(\frac{u_{*c}}{u_{*cw}}\ln\frac{12\delta_{cw}}{d_{50}} + \ln\frac{z}{\delta_{wc}}\right). \qquad (13)$$

Values of u_{*w} and u_{*c} are used to estimate a new value of C_r, until convergence. Grain roughness shear stress magnitudes are defined as $\tau_w = \rho u_{*w}^2$ and $\tau_c = \rho u_{*c}^2$ for wave and current, respectively.

3. Experiment Description

3.1. Field Site

[12] Study regions were on Sable Island Bank, a unique outer-shelf bank composed entirely of mobile sand. An instrument package called Ralph was deployed over several years at five sites (Figure 1). Table 1 lists mean water depths, experiment duration, grain sizes, and latitude/longitude coordinates. All sites are underlain by approximately 20 m of well-sorted Holocene sand, which forms a series of shoreface-connected sand ridges O(10) m in height and O(1) km in wavelength [*Amos et al.*, 1988]. Sediment grain size varies over the sand ridges: coarse sand in the troughs and lower western flank, medium sand on western flanks, and fine sand on the crests and eastern flanks. Sediment samples were collected at four of the five sites using Van Veen grabs (2001a, 1998b), or sediment traps (1997a, 1997c) located 0.3 m above the seafloor. Sediment grain diameters were estimated from mean phi ± 1 standard deviation. The mean phi value, x_φ, was estimated as

$$x_\varphi = \frac{\sum f m_\varphi}{100}, \qquad (14)$$

where f is the weight percent in each grain-size grade and m_φ is the midpoint of each grain-size grade in phi values. The standard deviation was estimated as

$$\sigma_\varphi = \sqrt{\frac{\sum f\left(m_\varphi - x_\varphi\right)}{100}}, \qquad (15)$$

and phi values were converted to diameter using

$$d_{50} = 2^{-x_\varphi}, \qquad (16)$$

$$d_{16} = 2^{-x_\varphi - \sigma_\varphi}, \qquad (17)$$

$$d_{84} = 2^{-x_\varphi + \sigma_\varphi}, \qquad (18)$$

where diameters are in millimeters. No sediment sample was collected from the 2000a site, and a median sediment grain diameter, d_{50}, of 125 μm has been assumed [*Amos and Nadeau*, 1988].

3.2. Instrumentation and Data Processing

[13] A three-dimensional (3-D) view of the instrument support frame is shown in Figure 2. The frame measured 2.6 × 3.3 × 2 m and housed four current meters, two rotary acoustic sonar (pencil-beam and a fan-beam), a digital video camera, pressure, tilt, roll, temperature, compass sensors, and up to four Acoustic Backscatter Sensors (ABS). The duty cycle for 2001a and 2000a was one burst every 2 hours, and one burst every hour for the other three experiments. Data from the digital video camera were not collected during all deployments. The instrument package has been discussed in some detail by *Heffler* [1996].

[14] Four Marsh-McBirney electromagnetic current meters (Model 523) measured two horizontal components

Table 1. Experiment Summary Information Including Designation by Year, Latitude, Longitude, Duration (in Days) of Good Quality Velocity Data, Average Water Depth, h, and Sediment Grain Diameters, d_{50}, d_{16}, and d_{84}

Experiment	Latitude	Longitude	Duration, days	h, m	d_{50}, μm	d_{16}, μm	d_{84}, μm
1997a	43°56′	60°38′	17	32	400	207	776
1997c	43°56′	60°38′	12	42	230	171	330
1998b	43°57′	60°05′	14	20	260	195	348
2000a	43°57′	59°41′	3	32	125	...	...
2001a	43°56′	60°33′	18	23	411	295	531

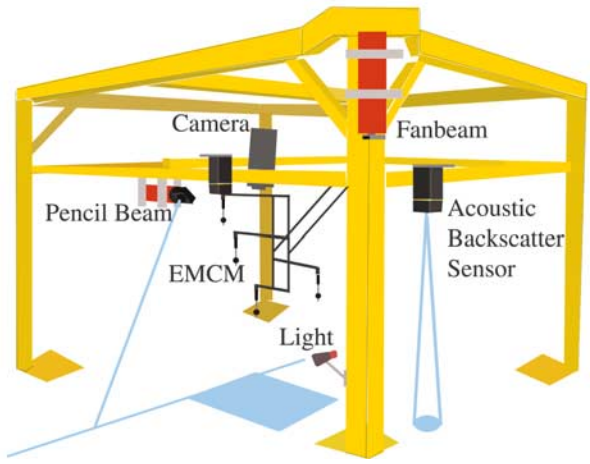

Figure 2. Three-dimensional view of the frame and instruments including approximate footprints for Acoustic Backscatter Sensors (ABS), pencil-beam sonar, and digital video camera. Pressure cases housing instrument electronics are not shown.

of fluid velocity at nominal heights of 0.3, 0.5, 0.7, and 1 m above the bed. Velocity measurements in this study used data from 1 m for 2001a and 0.7 m for the other four experiments. The distance to the seafloor varied with time depending on bedform migration and bed elevation changes. Measured velocities were rotated into an east-north coordinate system (relative to magnetic north) using the measured compass reading.

[15] Additional sensors (not shown in Figure 2) included pressure, pitch, roll, temperature, a compass, and six Optical Backscatter Sensors. The pressure sensor was a 500-psi Data Instruments transducer accurate to 0.08 m. Pitch and roll sensors were accurate to 0.1°. The fluxgate compass was calibrated on the frame to minimize interference and was accurate to 0.3°. Pressure and velocity data were collected at 5 Hz for 15 min using a Tattletale 5F. One estimate of pitch, roll, and heading was collected at the beginning of each burst.

[16] Bedform profiles were measured using a pencil-beam rotary sonar. A 0.675-MHz Imagenex sonar (Model 881P) was attached to the quad frame nominally 1.3 m above bottom and rotated about a horizontal axis through a sector width of approximately 120°. Data were acquired at an analog-to-digital conversion rate of 250 kHz at 12-bit resolution. The 500 1-cm range bins are comparable to the range resolution of 0.75 cm based on two-way travel time of a 10-μs pulse. The transducer head was rotated in 0.3° increments, smaller than the nominal angular width of the pencil-beam of 1.7°. One scan was collected per burst.

[17] Bed location was determined at each angle as the position where the backscatter amplitude exceeded 60% of the maximum. Bed elevation profiles were despiked, spatially smoothed (three-point moving average) and interpolated to a 1-cm grid. For small and medium wavelength bedforms (wavelength less than 1 m), bedform height was taken as $2\sqrt{2}\sigma_Z$, where σ_Z is the standard deviation of the seafloor elevation [*Smyth et al.*, 2002]. For larger bedforms, the number of bedforms covered by the pencil-beam was limited. Heights for large bedforms were estimated as the average difference in elevation from crest to trough. In four cases, the pencil-beam profile did not contain a bedform crest, and bedform height was interpolated from neighboring estimates.

[18] A 0.675-MHz Imagenex rotary fan-beam (Model 881) was attached to the frame leg nearest to the pencil beam, approximately 1.5 m above bottom. The fan-beam rotated 270° in 0.3° increments about a vertical axis. The beam width was 1.7° × 30°, and the range was set to 20 m with 500 range bins and a 1-m offset. Fan-beam data were corrected for time-variable gain and cleaned with a median filter (seven neighbors, 3 standard deviation threshold) to remove speckle noise. A fifth-order Coiflet wavelet was used to remove low-order background noise. One scan was collected per burst.

[19] For data with active bedforms, wavelength and direction were obtained by spectral analysis of the rotary fan-beam data following *Hay and Mudge* [2005]. Peak wave number was estimated from the power spectral density for each radial slice. For linear bedforms, the wave number is a maximum when the acoustic beam is orthogonal to the bedform crests and decreases as the cosine of the rotation angle. A full 360° would have two maxima indicating the direction of the bedforms (180° ambiguity) and two minima along the crests (90° from the maxima). With only 270° of data, usually one maximum or minimum was not present. Bedform direction was selected as the angle with the maximum spectral density and visually confirmed. Bedform wavelength was estimated as the inverse of the peak wave number in the bedform direction (defined crest-perpendicular). At times, bedforms were omni-directional and bedform wavelength was independent of rotation angle.

[20] Up to four acoustic backscatter sensors were attached to the frame, nominally 1.3 m above the seafloor. These 1-MHz sensors recorded 1 min. time series and were used to determine local seafloor elevation.

3.3. Forcing Time Series

[21] There were a total of 150 bursts which had good quality velocity data and well-formed bedforms. Figure 3 shows time series of wave and current speeds with selected bursts superposed. Wave velocity is defined as the measured velocity minus the mean (current) velocity. Selected time intervals were generally within wave-dominated storm events. However, there are some cases where currents were ~40 cm/s and wave energies were relatively small.

[22] Wave direction was estimated by rotating the two-axis coordinate system until the variance was maximized along one axis. Table 2 gives experiment-averaged significant wave velocities rotated in the wave direction and average current speeds. Significant wave height, h_s, was taken as 4 times the RMS elevation, and the significant wave velocity, $u_{1/3}$, was taken as $2u_{w_{rms}}$ where u_w has been rotated into the wave direction.

[23] The mobility number, ψ, is given by

$$\psi = \frac{u_{1/3}^2}{(s-1)gd_{50}}, \tag{19}$$

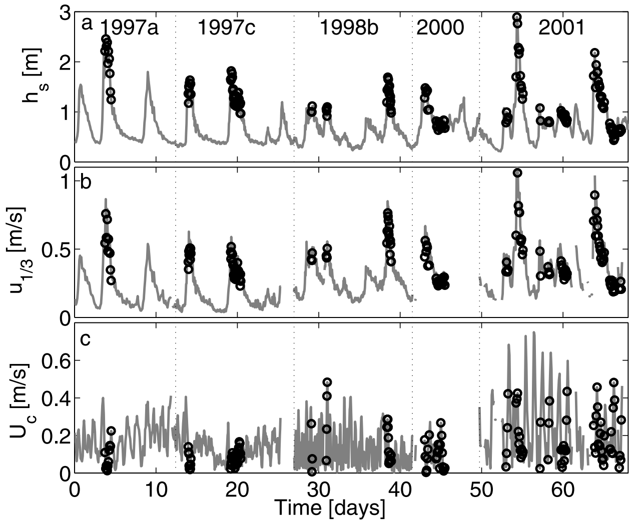

Figure 3. Concatenated time series of (a) significant wave height measured at depth, (b) significant wave velocity rotated in the wave direction, and (c) current speed. Circles indicate selected bursts. Time series start on yeardays 28.42, 102.83, 84.96, 110.42, and 17.50 in their respective years.

where s is the ratio of particle to fluid density. The wave Shields parameter is defined as

$$\theta_w = \frac{f_{ws}}{2}\psi, \tag{20}$$

where f_{ws} is the grain roughness wave friction factor obtained from *Swart* [1974],

$$f_{ws} = \exp\left[5.213\left(\frac{2.5d_{50}}{A}\right)^{0.194} - 5.977\right], \tag{21}$$

where A is the wave orbital semi-excursion. The current Shields parameter has a similar expression,

$$\theta_c = \frac{0.006U_c^2}{(s-1)gd_{50}}, \tag{22}$$

where a constant friction factor is assumed [*Sternberg*, 1972]. The wave orbital semi-excursion is given by

$$A = u_{1/3}/\omega, \tag{23}$$

where ω is the energy-weighted angular frequency. The wave orbital excursion, d_0, is twice this value.

4. Bedform Observations

4.1. Bedform Type

[24] Bedforms were roughly separated into five types: wave ripples (W), wave ripples with subordinate current ripples (W_c), combined wave-current ripples (WC), current ripples with subordinate wave ripples (C_w), and current ripples (C), following *Amos et al.* [1988]. They found good segregation of different bedform types using a current Shields parameter [*Sternberg*, 1972] and a modified wave Shields parameter [*Grant and Madsen*, 1979]. Figure 4 shows present values of current Shields parameter and modified wave Shields parameter from the BLASST model along with approximate divisions from *Amos et al.* [1988]. BLASST refers to the Boundary Layer Stress and Sediment Transport model and has extended the model by *Grant and Madsen* [1979] to include a broader range of eddy viscosity profiles [*Styles and Glenn*, 2002]. Present observations show a wide range of bedform types, but about 70% of the data were in two categories: wave ripples and wave ripples with subordinate current ripples.

Table 2. Forcing Parameters for Selected Bursts in Each Experiment Including Significant Wave Velocity, Current Speed, and T, the Energy-Weighted Wave Period, All Averaged Over the Number of Selected Bursts, N_B[a]

Experiment	$u_{1/3}$, cm/s	U_c, cm/s	T, s	N_B
1997a	52.3 (4.7)	9.2 (2.2)	9.6	10
1997c	37.6 (1.3)	7.9 (0.6)	10.5	40
1998b	54.2 (2.5)	16.6 (2.8)	9.0	21
2000a	33.2 (2.4)	9.9 (1.6)	10.0	21
2001a	45.4 (2.8)	19.0 (1.7)	9.5	58

[a]Standard error is given in brackets.

[25] Most of the observed bedforms from *Amos et al.* [1988] were current ripples and current ripples with subordinate wave ripples. Noting that both experiments were conducted on Sable Island Bank at similar water depths, this difference may be surprising. However, the instrumentation used in the two experiments resolves different scales: Photographs from *Amos et al.* [1988] could detect a minimum wavelength of a few centimeters and a maximum wavelength of ~1 m; rotary sonars used in the present experiment have a much larger range and can easily detect medium and large bedforms. Therefore, present observations should be considered complementary to previous small scale bedform observations.

4.2. Bedform Dimensions

[26] In this section, bedform height and wavelength are presented and compared to previous observations of wave

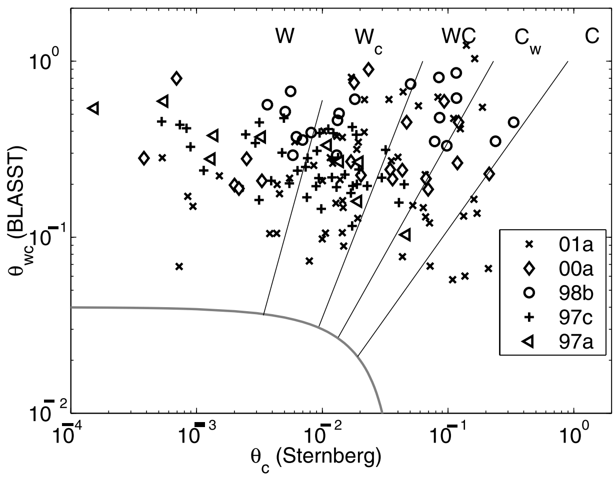

Figure 4. Scatterplot of wave-current Shields parameter (BLASST) versus current Shields parameter for selected bursts. Also shown are approximate bed form type divisions.

Table 3. Averaged Bed Form Height and Wavelength for Each Experiment[a]

Experiment	η, cm	λ, cm
1997a	13 (1)	176 (4)
1997c	13 (0.2)	100 (2)
1998b	9 (0.8)	99 (7)
2000a	7 (0.2)	60 (4)
2001a	10 (0.7)	81 (4)

[a]Standard error is given in brackets.

and wave-current ripples. In order to avoid hysteresis effects, 26 out of 150 cases were removed where the orbital excursion and current speed decreased without a corresponding decrease in bedform wavelength. The average observed bedform wavelength for 124 bursts was 92 cm (standard error of 3 cm). The maximum observed bedform wavelength during the 2001a and 1997a experiments was 1.9 m. Current speeds at maximum bedform wavelength were ~40 cm/s and ~20 cm/s for the two experiments, respectively. In both cases the maximum bedform wavelength occurred just after storm peak when the orbital excursion was decreasing. Table 3 lists experiment-averaged bedform dimensions.

[27] Typically, bedform dimensions are normalized and plotted as a function of mobility number to simplify data comparison. Figure 5 shows bedform dimensions normalized by the wave orbital semi-excursion. Also shown are data for three bedform types from two nearshore experiments [*Smyth and Hay*, 2003; *Smyth et al.*, 2002], and other field observations parameterized by *Nielsen* [1992, p. 137, 143]. These observations are of nearshore wave ripples and include suborbital ripples, anorbital ripples, and orbital ripples [*Clifton and Dingler*, 1984]. Present observations of bedform heights and wavelengths are generally larger than nearshore estimates of wave ripples.

[28] Another normalization suggested by *Khelifa and Ouellet* [2000] uses an effective fluid displacement distance during a wave period, d_{wc}, estimated from vectorially added wave and current displacements,

$$d_{wc} = \sqrt{d_0^2 + (TU_c)^2 + 2d_0(TU_c)|\cos\phi|}, \qquad (24)$$

where ϕ is the angle between the wave and current vectors and T is the energy-weighted period (Table 2). The combined wave-current velocity, u_{wc}, defined as

$$u_{wc} = d_{wc}/T = \sqrt{\frac{u_{wo}{}^2}{\pi} + U_c^2 + 2U_c\frac{u_{wo}}{\pi}|\cos\phi|}, \qquad (25)$$

is used to estimate the wave-current mobility number, ψ_{wc}. Figure 6 shows the bedform dimensions normalized by wave-current parameters. There is much better grouping of the data and close agreement with the fit by *Khelifa and Ouellet* [2000]. Their fit is based on available data compiled from their laboratory data, and other laboratory and field results.

[29] Several authors have suggested a linear relation between ripple wavelength and wave orbital diameter for orbital ripples, ranging from 0.65 [*Miller and Komar*, 1980] to 1 [*Inman*, 1957]. Fitting the observed wavelengths for experiments 1998b and 2001 for 44 cases where $d_0/\eta < 20$ (orbital ripples) gives $\lambda/d_{50} = 0.33d_0/d_{50}$ with $R^2 = 0.62$.

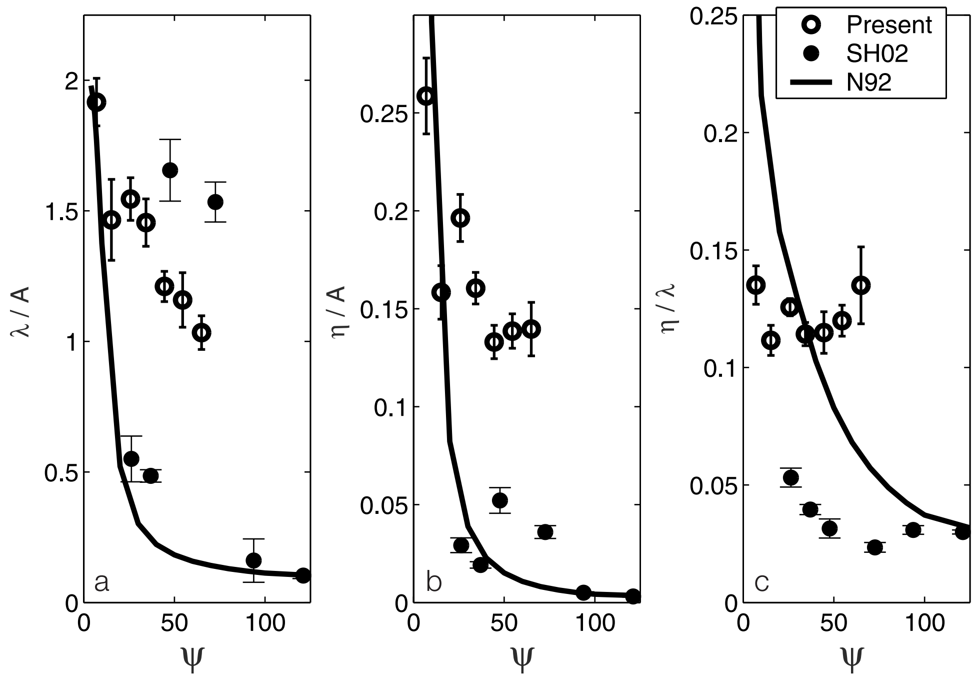

Figure 5. Bin-averaged (a) normalized bed form wavelength, (b) normalized bed form height, and (c) bed form steepness as a function of mobility number. Error bars indicate standard error. Also shown for comparison are nearshore measurements by *Smyth and Hay* [2002] and predictions by *Nielsen* [1992, equations (3.4.3) and (3.4.8)].

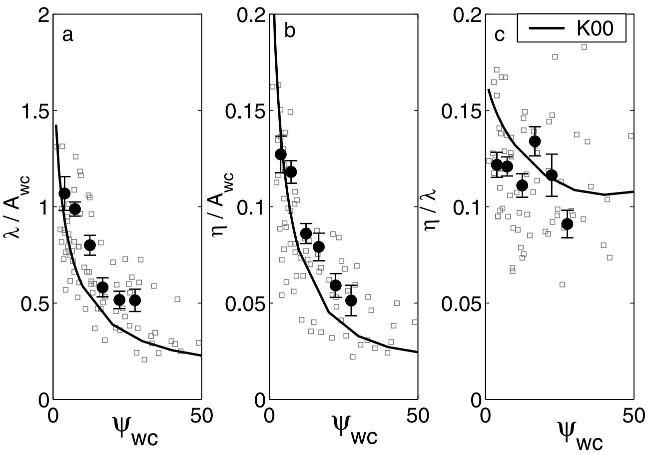

Figure 6. (a) Bed form wavelength and (b) height normalized by half the effective fluid displacement distance. (c) Bed form steepness as a function of wave/current mobility number. Burst data are indicated by small squares, and bin-averaged data and standard error are indicated by circles. Fits by *Khelifa and Ouellet* [2000] are indicated by the solid line.

This slope is the similar to the value of 0.38 found by *Traykovski et al.* [1999] for 3-D bedforms at relatively low wave energies in 15 m water depth. The correlation between λ/d_{50} and d_{wc}/d_{50} is poor ($R^2 = 0.1$) when the effective fluid displacement is used. Similarly, the correlation between λ/d_{50} and ψ is fair ($R^2 = 0.49$) but drops when ψ_{wc} is used ($R^2 = 0.09$). As λ is neither correlated with d_{wc} nor ψ_{wc}, but d_{wc} is well correlated with ψ_{wc} ($R^2 = 0.92$), perhaps there is a spurious correlation which is causing a collapse of the data in Figure 6.

[30] The maximum bedform wavelength of 1.9 m is almost 4 times higher than nearshore predictions by *Wiberg and Harris* [1994] when d_{50} is used and 2 times higher when d_{84} is used. *Traykovski et al.* [1999] also found a larger than predicted bedform wavelength (1 m) in 15 m water depth. They hypothesized that long-period low-velocity waves at deeper locations cause predominantly bedload transport which favors orbital scale ripples. In shallower locations, high-velocity short-period waves result in suspended load transport which favors anorbital ripples or sheet-flow conditions. As the water depth for 2001a is 23 m, a longer maximum bedform wavelength is not unexpected. One could further hypothesize that the current would also favor bedload transport, in which case, bedform wavelengths would be larger than predicted by wave-only conditions. The contribution from the tidal current is not well understood and requires further investigation.

4.3. Bedform Direction

[31] Bedform direction, defined as orthogonal to bedform crests, was estimated for all selected bursts to determine if bedforms were aligned with the waves or were rotating with the tidal currents. For 30 of the 150 bursts, bedforms were omni-directional or bidirectional and were not considered. Figure 7 shows wave, current, and bedform direction versus Shields parameters (equations (20) and (22)). The bedform direction distribution is more closely related to the wave direction distribution than to the current direction distribution. Also shown in this figure is a histogram of the differences between bedform direction (ϕ_r) and wave direction (ϕ_w) and current direction (ϕ_c). The average difference between bedform and wave directions is 1.3° with a standard error of 2.1°. The average difference between bedform and current directions is much larger: 12.3° ± 4.8°.

[32] Additionally, observations showed that bedforms had a tendency to respond to relatively small changes in wave direction, but not to the rotating tidal current. Photographs of small current bedforms in the 1997a experiment showed migration in the direction of the rotating current, but these were small (~10 cm wavelength), short-crested arcuate ripples which would facilitate abrupt changes in migration direction. The medium and large wavelength bedforms observed by the rotary sonar were quasi-linear and were not observed to rotate with the current. As these bedform are relatively large, perhaps the constantly changing direction of the tide did not allow enough time for the bedforms to adjust.

5. Bedform Migration

5.1. Measured Bedform Migration

[33] Bedform migration velocity was estimated from 1-D cross correlations of windowed rotary fan-beam data. Windows were nominally 12 × 11 m and were aligned with bedform direction. Migration rates were calculated by estimating the average cross-correlation displacement between two sequential images and dividing by the time between bursts (every hour in 1997 and every 2 hours in 2001). Cases where the bedforms evolved substantially between bursts were not considered. Observations from five time intervals were selected for comparison with model predictions. Two of these intervals were from the 1997c experiment, and the other three were from 2001a. These intervals include a total of 70 estimates of migration rate, of which 30 were from the spin-down of the second storm of 1997c on yearday 109. Figure 8 shows bedform migration

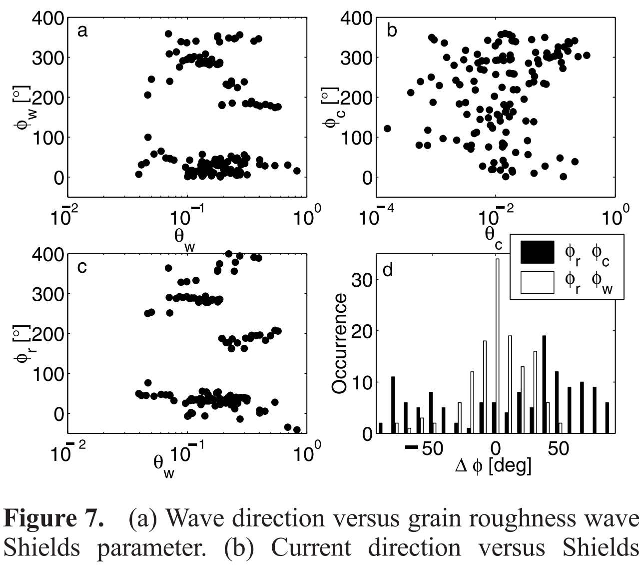

Figure 7. (a) Wave direction versus grain roughness wave Shields parameter. (b) Current direction versus Shields parameter. (c) Bed form direction versus grain roughness wave Shields parameter. (d) Histogram of the angle difference, $\Delta\phi$, between bed form and wave direction (white) and bed form and current direction (black).

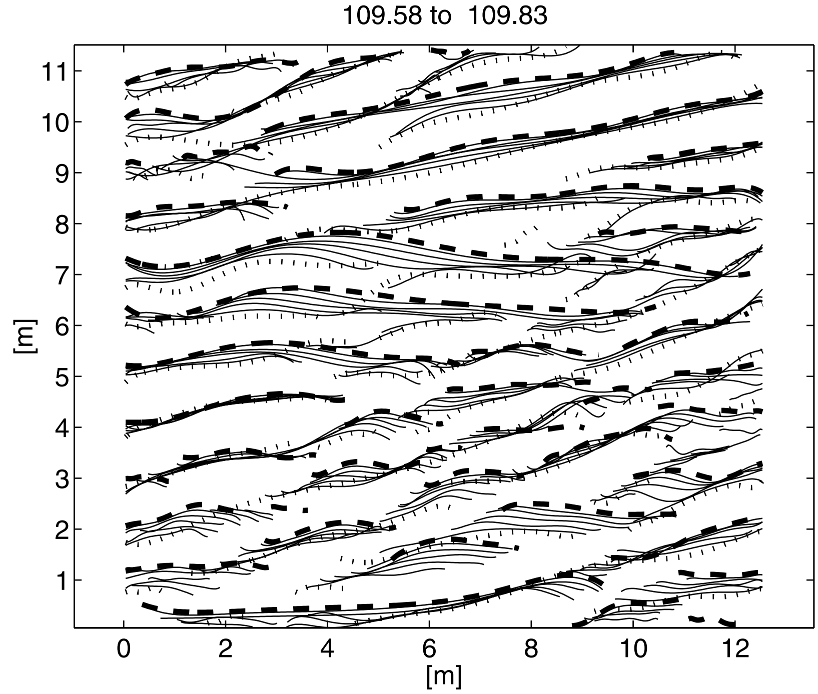

Figure 8. Bed form crest positions for a windowed section of data from 1400 to 2000 local time on yearday 109. Initial and final positions are indicated by the dotted and dashed lines, respectively, with hourly positions denoted using solid lines. The window is centered about a bed form direction of 130°.

from a short section of this storm. Bedforms moved upward and to the right, with a maximum displacement of ~0.5 m, although some bedforms (i.e., lower left corner) moved very little. Bedform crest positions for this figure were determined using an automatic crest detection routine which is described in Appendix A.

[34] Figure 9 shows the migration rates as well as current and wave velocities for 30 hours on yearday 109. Migration was generally in the direction of the waves, and large migration rates occurred when waves and currents formed acute angles. Small migration rates occurred when waves and currents were perpendicular, and reverse migration occurred when currents were opposite to the wave direction. This figure also shows velocity skewness, which is defined and discussed later in section 5.3.

[35] Vector correlation amplitudes between observed migration rates and velocity forcing had higher amplitudes for significant wave velocity than for current velocity. Velocity vector correlation coefficients are $R_k = r\exp(i\gamma)$ where r is the amplitude (product of the amplitude of the two vectors) and γ represents a speed-weighted estimate of the mean angle through which the test vector would have to be rotated counterclockwise to match the observed vector [*Kundu*, 1976]. A perfect correlation would have an amplitude of 1 and an angle of 0 (r = 1, γ = 0). Correlation coefficients between $\boldsymbol{U_m}$ and $\boldsymbol{u_w}$ were (0.75, 52°) and between $\boldsymbol{U_m}$ and **U** were (0.41, 25°).

5.2. Comparison to Model Predictions

[36] Three models were selected for comparison to the migration rate observations. Predicted bedload transport rates were converted to migration rates (equation (1)) using measured bedform heights and a sediment porosity of 0.4. Common model inputs included wave and current velocity, wave period, and sediment grain size.

[37] The first model, NH04, used wave orbital velocity amplitudes, u_{wo}, calculated using velocity peak and trough amplitudes (their second method). Friction factors were determined by comparing predicted and measured migration velocities (similar to their method). The ratio f_w/f_c was chosen to give the highest vector correlation amplitude between measured and predicted migration rates. Using this ratio, f_c was chosen such that the slope of measured versus

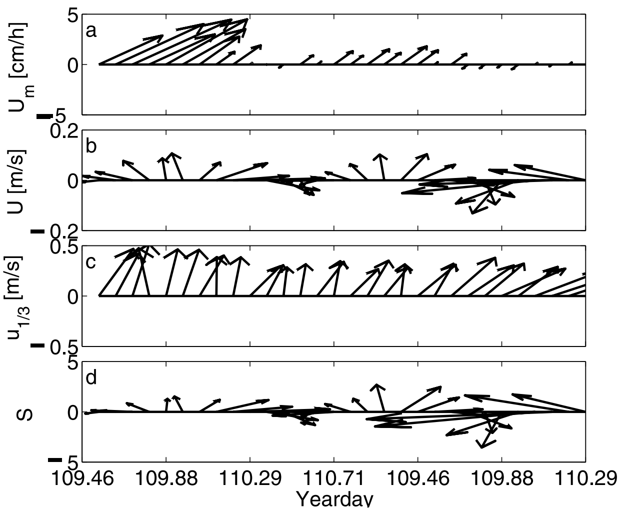

Figure 9. The 1997c time series of (a) bed form migration velocity, (b) current velocity, (c) significant wave velocity, and (d) skewness.

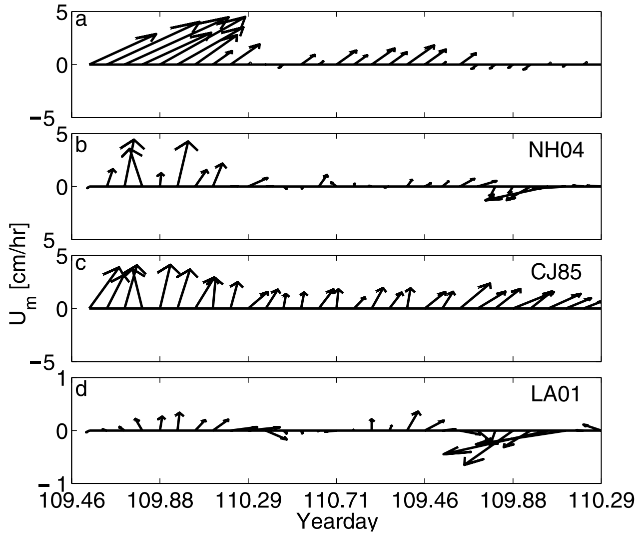

Figure 10. The 1997c time series of (a) measured bed form migration velocity, and predicted migration rates from (b) *Ngusaru and Hay* [2004], (c) *Christoffersen and Jonsson* [1985], and (d) *Li and Amos* [2001].

predicted migration rates (component in the bedform direction) was closest to 1.

[38] The second model, CJ85 (their turbulence model II), iteratively solves for friction factors until convergence. Wave amplitude was taken as $\langle u_{wo} \rangle$, and bedload transport rate was assumed to be proportional to $\tau^{3/2}$ (equation (2)). The third model, LA01, assumed an initial bedform height of 1.4 cm and a bedform wavelength of 12.2 cm for the 1997c experiment, and used estimated bedform heights and wavelengths for the 2001a data set.

[39] Predictions of bedform migration rates on yearday 109 are shown in Figure 10. Predictions were generally consistent with the observations during the first tidal cycle and showed high migration rates when currents were aligned with the waves. During the second tidal cycle, there was less consistency between predictions and observations. The LA01 model predicted large migration rates in the direction of the current which were not observed. The CJ85 model predicted persistent migration in the wave direction which was not observed. The NH04 model missed some migration in the direction of the wave, and predicted larger migrations in the direction of the current. Vector correlation amplitudes were highest for the CJ85 predictions (0.85), followed by NH04 predictions (0.68), and lowest for LA01 predictions (0.49), although the angle error decreased with decreasing correlation amplitude (38°, 25°, and 11°, respectively).

Table 4. Vector Addition of the Observed and Predicted Migration Velocities for the Five Selected Time Intervals[a]

Interval	Time	U_N or β_N	Measurement	NH04	CJ85	LA01
a	27.58	U_N	0.8	6.7	46.3	7.5
01a	28.25	β_N	−67	−53	−59	−56
b	31.92	U_N	7.4	38.9	95.1	117.9
01a	32.83	β_N	24	−25	23	−40
c	33.50	U_N	1.7	2.3	16.6	41.4
01a	34.00	β_N	−146	−19	29	−23
d	104.38	U_N	8.7	20.5	21.8	14.6
97c	104.71	β_N	33	165	41	173
e	109.50	U_N	42.7	19.3	64.7	8.1
97c	112.00	β_N	28	−3	12	−99

[a]Summed migration magnitude, U_N, is in cm/hr, and direction, β_N, is in degrees.

[40] Observed and predicted migration velocities were vectorially added for all five time intervals to produce a net migration rate (Table 4). Clearly, the models do not consistently predict net migration rates, and predictions vary substantially from model to model. Predicted directions of the net rates are also varied, with similarities between LA01 and NH04 results, and similarities between CJ85 results and the measurements.

[41] Two adjustable parameters in these models are the wave and current friction factors. As these parameters have not been measured for irregular waves and tides, comparison of the friction factors may provide insight into model predictions. Figure 11 shows the friction factors as well as the range of U_c and $u_{1/3}$ for the selected time intervals. Values of $U_c/u_{1/3}$ are generally less than 1, indicating a dominance of wave velocities.

[42] The LA01 model predicts values of f_w similar to CJ85. Estimates from NH04 have almost a decadal range in f_w with a maximum of ~0.02. Shown for comparison are wave friction factors predicted by *Tolman* [1994] which were found to be consistent with nearshore turbulence measurements by *Smyth and Hay* [2002] for irregular wave conditions. Surprisingly, all but one estimate from three models are lower than predictions by *Tolman* [1994]. Observations by van Doorn (cited by *Nielsen* [1992, p. 72]) in the laboratory have shown that the addition of a current does not decrease the turbulence in the wave bottom boundary layer. Thus wave friction factors for all three models are lower than expected.

[43] Current friction factors are highest for LA01, and are 3 times higher than predictions from CJ85, and higher than a skin friction factor of 0.006 [*Sternberg*, 1972]. These high values partially explain why bedforms were predicted to migrate in the direction of the current in the LA01 model.

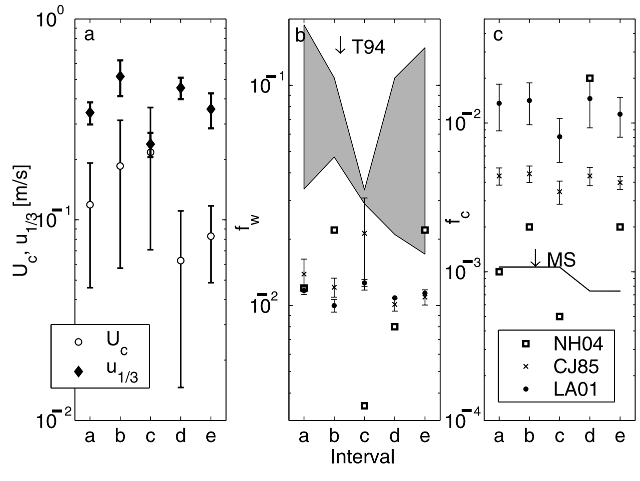

Figure 11. Averaged (a) measured U_c and $u_{1/3}$ for the selected time intervals, (b) combined wave-current friction factors, and (c) current friction factors. Friction factors from *Tolman* [1994] and Manning-Strickler are also shown. Error bars and shading indicate the standard deviation.

The range of current friction factors in the CJ85 model is narrow (~0.01), possibly because this equation contains the water depth (equation (6)) which is fairly large. Current friction factors for the NH04 model have a decadal range, and some are below skin friction factors predicted by the Manning-Strickler formula [*Sleath*, 1984, p. 220] for flat immobile beds in the absence of waves.

5.3. Skewness

[44] Wave skewness has compared favorably to bedform migration in previous studies [*Traykovski et al.*, 1999; *Crawford and Hay*, 2001]. For the present observations, the tidal current was included in the skewness by defining a skewness vector, $\mathbf{S} = (S_x, S_y)$:

$$S_x = \left\langle (u_{wx} + U_c \cos\phi_c)^3 \right\rangle / \sigma^3_{u_{wx}} \tag{26}$$

$$S_y = \left\langle (v_{wy} + U_c \sin\phi_c)^3 \right\rangle / \sigma^3_{v_{wy}}, \tag{27}$$

where ϕ_c is the current direction, σ is the RMS velocity, and $\langle\ \rangle$ represents a time average. Skewness vectors, shown earlier for time interval "e" in Figure 9, were strongly controlled by the rotating tidal velocity vector. Vector correlation coefficients between skewness and currents were above 0.9 with angle error less than 15°. The largest contribution to the skewness magnitude was from the cross component (roughly 60%), followed by the current component (roughly 35%), with only a small contribution from the wave component (roughly 5%). The total skewness correlated poorly with migration rates (Table 5).

[45] Consider the component of the skewness parallel to the wave direction, S_p,

$$S_p = \left[\langle u_w^3\rangle + 3\langle u_w^2\rangle U_c \cos\phi + U_c^3 \cos^3\phi\right] / \sigma^3_{u_w}, \tag{28}$$

where u_w is the wave velocity rotated into the wave direction, and ϕ is the angle between the waves and the currents. The first term on the right-hand side, say S_1, is the traditional wave skewness, the second, S_2, is the cross component, and the third term, S_3, is the current skewness. Migration velocities may be compared directly to S_p if the angle between the wave direction and the bedform direction is ignored. Figure 12 shows regressions of migration velocity and wave parallel skewness. There was poor agreement between traditional wave skewness, S_1, and measured migration rates (R^2 = 0.22), consistent with previous combined-flow results [*Ngusaru and Hay*, 2004].

Table 5. Vector Correlation Amplitudes, r, and Angles, γ (in Degrees), for Migration Velocities and Forcing Time Series for Time Interval "e"

	U_m	$u_{1/3}$	U	S
Measurement r	0.75	0.41	0.29	
Measurement γ	52	25	10	
NH04 r	0.60	0.57	0.47	
NH04 γ	39	−5	−13	
CJ85 r	0.93	0.30	0.27	
CJ85 γ	12	−47	−77	
LA01 r	0.50	0.89	0.89	
LA01 γ	78	−3	−6	

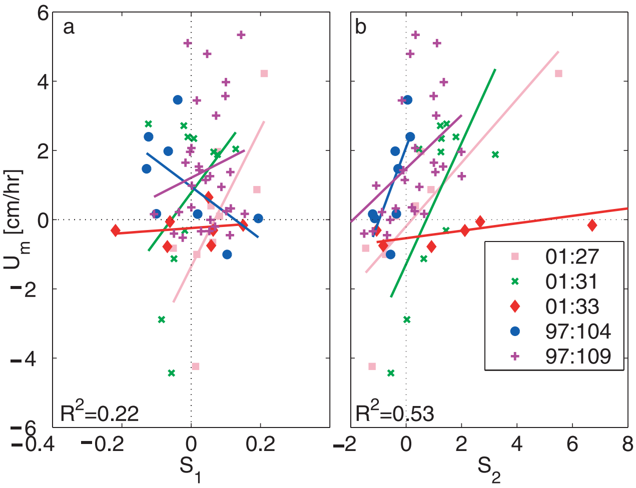

Figure 12. Regressions of bed form migration velocity and (a) normalized wave skewness and (b) cross component of the skewness. Five time intervals "a" through "e" (year:yearday) are indicated by the symbols and color-coded regression lines.

However, a higher correlation was found (R^2 = 0.53) between observed migration rates and S_2.

6. Discussion

[46] Migration rate measurements did not agree with wave skewness or total skewness, but poor agreement may be expected as large water depths preclude shoaling which causes high wave skewness and/or wave asymmetry. Better agreement is found between measured migration rates and wave-current skewness in the direction of the waves. The reason for this agreement may be related to the orientation of the bedforms relative to the current direction. When the current is flowing over the bedform crests the friction should be larger than when the current is flowing along the troughs/crest. In this study, bedforms were predominantly aligned with the waves, and thus the bed friction (and migration rates) should increase when waves and currents are aligned.

[47] None of the models incorporate bedform direction, and therefore cannot explicitly alter the friction factor when the current is aligned with bedform direction. As an approximation, models could assume that bedforms were aligned with the waves, and could define friction factors as a function of the angle between waves and currents. This may reduce LA01 predicted migration rates in the current direction, and may reduce the scatter in the NH04 friction factors.

[48] Note that migration rate results are based on 70 estimates from two experiments. More measurements are needed to verify these findings, and direct measurements of turbulence intensity are needed to constrain the range of friction factors.

7. Conclusions

[49] Medium and large bedforms on Sable Island Bank were primarily wave and wave-current bedforms based on the stress analysis following *Amos et al.* [1988] and

were observed to be predominantly aligned with the waves.

[50] Normalized bedform dimensions were larger than previous nearshore observations of wave bedforms, suggesting the influence of long-period waves and currents. Modifying bedform normalization to include current effects collapsed the data and was consistent with laboratory observations from *Khelifa and Ouellet* [2000]. The scale between bedform wavelength and wave orbital excursion was 0.33 for 44 wave orbital bedform cases from experiments 1998b and 2001. This scale is similar to the value of 0.38 from *Traykovski et al.* [1999] for 3-D ripples.

[51] Bedforms migrated primarily in the direction of the waves, but at times reversed direction when the current was 180° to the waves. Predictions from three models were compared to migration rate estimates. The CJ85 model was dominated by wave forcing, the LA01 model was dominated by current forcing, and the NH04 model included effects from both waves and currents. The three models showed a large range in both wave and current friction factors, which suggests that accurate measurements of friction factors would likely improve model results.

[52] Total skewness was dominated by the current, and was poorly correlated with migration rates. Wave skewness, estimated in the wave direction, was also poorly correlated with migration rates. However, the component of the total skewness in the wave direction had better agreement with migration rates.

Appendix A: Crest Identification Method

[53] An automatic crest identification procedure was developed using Matlab's image processing toolbox to locate and fit bedforms crests. Windowed sections of fan-beam data were selected according to bedform orientation. Top-hat and bottom-hat filtering was used to separate crests from troughs by making crests larger and troughs deeper. These filters used a disk structure function with a radius of 12 range bins. Next, an edge detection algorithm (Canny method) was used to find local maxima in the amplitude gradient. Edges near the low threshold were only included if connected to an edge close to the high threshold. After this step, the data consisted of a binary array with detected edges separating bedform crests from bedform troughs. To identify the position of the crests, amplitude values from the original data were determined between detected successive edges in the direction of the bedforms. Areas above a threshold of 1.5 times the median were defined to be bedform crests. Several morphological binary operations were used to correct small errors: bridging removed isolated 0-valued bins, cleaning removed isolated 1-valued, morphological erosion and dilation removed errant tails, and filling of holes in an eight-bin connected neighborhood removed gaps within the bedform crests. Finally, seventh-order polynomials were fitted to individual bedform crests.

[54] **Acknowledgments.** The authors would like to thank Geological Survey of Canada- Atlantic coworkers Dave Heffler, Tony Atkinson, Bob Murphy, Fred Jodrey, Angus Robertson, Ken Aspery, Donny Clattenburg, and Owen Brown for providing excellent technical, field, and laboratory assistance. Thanks are also owed to Bob Courtney for providing instruction on wavelet denoising, and to Alex Hay and two anonymous reviewers for providing insightful comments which improved the manuscript. This paper is Geological Survey of Canada contribution 2004092.

References

Amos, C. L., and O. Nadeau (1988), Surficial sediment character on Sable Island Bank and Banquereau, Scotian Shelf, Canada, *Can. J. Earth Sci.*, *25*(12), 1923–1944.

Amos, C. L., A. J. Bowen, D. A. Huntley, and C. F. Lewis (1988), Ripple generation under the combined influences of waves and currents on the Canadian continental shelf, *Cont. Shelf Res.*, *8*(10), 1129–1153.

Bagnold, R. A. (1946), *The Physics of Blown Sand and Desert Dunes*, 265 pp., CRC Press, Boca Raton, Fla.

Brown, C. B. (1950), Sediment transport, in *Engineering Hydraulics*, edited by H. Rouse, pp. 769–857, John Wiley, Hoboken, N. J.

Christoffersen, J. B., and I. G. Jonsson (1985), Bed friction and dissipation in a combined current wave motion, *IEEE J. Oceanic Eng.*, *12*, 387–423.

Clifton, H. E., and J. R. Dingler (1984), Wave-formed structures and paleoenvironmental reconstruction, *Mar. Geol.*, *60*, 165–198.

Crawford, A. M., and A. E. Hay (2001), Linear transition ripple migration and wave orbital velocity skewness: Observations, *J. Geophys. Res.*, *106*(C7), 14,113–14,128.

Gallagher, E. L., S. Elgar, and E. B. Thornton (1998), Megaripple migration in a natural surf zone, *Nature*, *394*, 165–168.

Grant, W. D., and O. S. Madsen (1979), Combined wave and current interaction with a rough bottom, *J. Geophys. Res.*, *84*(C4), 1797–1808.

Grant, W. D., and O. S. Madsen (1986), The continental shelf bottom boundary layer, *Ann. Fluid Dyn.*, *18*, 265–305.

Hay, A. E., and T. D. Mudge (2005), Principal bed states during SandyDuck97: Occurrence, spectral anisotropy, and the bedstate storm cycle, *J. Geophys. Res.*, doi:10.1029/2004JC002451, in press.

Heffler, D. E. (1996), A dynamic instrument for sediment dynamics, paper presented at Oceans '96, Inst. of Electr. and Electron. Eng., New York.

Inman, D. L. (1957), Wave generated ripples in nearshore sands, technical report, Beach Erosion Board, U. S. Army Corps of Eng., Washington, D. C.

Khelifa, A., and Y. Ouellet (2000), Prediction of sand ripple geometry under waves and currents, *J. Waterw. Port Coastal Ocean Eng.*, *126*, 14–22.

Kundu, P. (1976), An analysis of inertial oscillations observed near the Oregon coast, *J. Phys. Oceanogr.*, *6*, 879–893.

Li, M. Z., and C. L. Amos (2001), SEDTRANS96: The upgraded and better calibrated sediment-transport model for continental shelves, *Comput. Geosci.*, *27*, 619–645.

Li, M. Z., C. L. Amos, and D. E. Heffler (1997), Boundary layer dynamics and sediment transport under storm and non-storm conditions on the Scotian Shelf, *Mar. Geol.*, *141*, 157–181.

Madsen, O. S., and W. D. Grant (1976), Quantitative description of sediment transport by waves, paper presented at 15th Coastal Engineering Conference, Am. Soc. of Civ. Eng., New York.

Miller, K. S., and P. D. Komar (1980), A field investigation of the relationship between ripple spacing and near-bottom water motions, *J. Sediment. Petrol.*, *50*, 183–191.

Ngusaru, A. S., and A. E. Hay (2004), Cross-shore migration of lunate megaripples during Duck94, *J. Geophys. Res.*, *109*, C02006, doi:10.1029/2002JC001532.

Nielsen, P. (1992), *Coastal Bottom Boundary Layers and Sediment Transport*, 324 pp., World Sci., Hackensack, N. J.

Sleath, J. F. A. (1984), *Sea Bed Mechanics*, John Wiley, Hoboken, N. J.

Sleath, J. F. A. (1995), Sediment transport by waves and currents, *J. Geophys. Res.*, *100*(C6), 10,977–10,986.

Smyth, C., and A. E. Hay (2002), Wave friction factors in nearshore sands, *J. Phys. Oceanogr.*, *32*, 3490–3498.

Smyth, C., and A. Hay (2003), Near-bed turbulence and bottom friction during SandyDuck97, *J. Geophys. Res.*, *108*(C6), 3197, doi:10.1029/2001JC000952.

Smyth, C., A. Hay, and L. Zedel (2002), Coherent Doppler profiler measurements of near-bed suspended sediment fluxes and the influence of bedforms, *J. Geophys. Res.*, *107*(C8), 3105, doi:10.1029/2000JC000760.

Sternberg, R. W. (1972), Predicting initial motion and bedload transport of sediment particles in the shallow marine environment, in *Shelf Sediment Transport, Process and Pattern*, edited by D. J. Swift, D. B. Duane, and O. H. Pilkey, pp. 61–83, Dowden and Hutchinson and Ross, Stroudsburg, Pa.

Styles, R., and S. M. Glenn (2002), An optimized combined wave and current algorithm for arbitrary bed roughness, technical report, Univ. of S. C., Columbia.

Swart, D. H. (1974), Offshore sediment transport and equilibrium beach profiles, *Tech. Rep. 131*, Delft Hydraulics Lab., Delft, Netherlands.

Tolman, H. L. (1994), Wind waves and movable-bed bottom friction, *J. Phys. Oceanogr.*, *24*, 994–1009.

Traykovski, P., A. E. Hay, J. D. Irish, and J. R. Lynch (1999), Geometry, migration and evolution of wave orbital ripples at LEO-15, *J. Geophys. Res.*, *104*(C1), 1505–1524.

Wiberg, P. L., and C. K. Harris (1994), Ripple geometry in wave-dominated environments, *J. Geophys. Res.*, *99*(C1), 775–789.

M. Z. Li, Bedford Institute of Oceanography, Geological Survey of Canada–Atlantic, Dartmouth, NS, B2Y 4A2, Canada. (mli@nrcan.gc.ca)

C. E. Smyth, Department of Oceanography, Dalhousie University, Halifax, NS, B3H 4J1, Canada. (carolyn.smyth@phys.ocean.dal.ca)